## ARTICLE

**Open Access**

# Wearable multifunctional soft sensor and contactless 3D scanner using supersonically sprayed silver nanowires, carbon nanotubes, zinc oxide, and PEDOT:PSS

Hong Seok Jo[1,2,3], Chan-Woo Park[1], Seongpil An [2,4], Ali Aldalbahi[5], Mohamed El-Newehy[5], Simon S. Park[3], Alexander L. Yarin [1,6] and Sam S. Yoon [1]

### Abstract

The multifunctional soft sensor developed here is capable of simultaneously sensing six stimuli, including pressure, bending strain, temperature, proximity, UV light, and humidity, with high accuracy and without interference among the respective built-in components. The sensor is fabricated via a facile, scalable, and cost-effective supersonic cold-spraying method using silver nanowires (AgNWs), carbon nanotubes (CNTs), zinc oxide (ZnO), and conducting polymer poly(3,4-ethylenedioxythiophene) polystyrene sulfonate (PEDOT:PSS). A mask and laser cutter are used in conjunction with the supersonic cold-spraying method to produce miniaturized multifunctional sensors that can be readily installed on various substrates; for example, the production of gloves capable of multifunctional sensing. In particular, the proximity sensor of the multifunctional glove sensor can produce a three-dimensional (3D) image of a scanned object, showing high potential for use in military, medical, and industrial applications.

## Introduction

Based on the approaches underpinning the Fourth Industrial Revolution (4IR), tremendous progress has been made in technological convergence, which has led to remarkable developments in science and technology in this period of human history. In particular, the Internet of Things (IoTs) has resulted in the fusion of cyber and physical domains, and it is currently ushering in significant improvements to human life by facilitating real-time communication between electronics and computer networks based on high-tech interface systems[1,2]. Accordingly, the demand for high-tech interface systems has enormously increased, prompting the development of advanced artificial electronic skin (e-skin) that can monitor the internal or external conditions of human skin in real-time.

As a multifunctional soft sensor, artificial e-skin not only requires flexibility, multifunctionality, and wearability (or attachability to body contours) but should also be able to respond to various stimuli, including pressure, temperature, approaching objects, humidity, and ultraviolet (UV) light, by converting these stimuli into electrical signals[3]. In particular, such an e-skin should be able to operate on highly curved or complex surfaces whose geometry may change over time, such as human fingers, elbows, and knees, to promote its potential use in humanoid robots[4], medical prostheses[5], and health care devices[6]. The e-skin should also be capable of conducting multiple tasks and performing simultaneous detection without interference among the functional components.

The practical usefulness of previously developed multifunctional sensors is limited because of their restricted

Correspondence: Seongpil An (esan@skku.edu) or
Alexander L. Yarin (ayarin@uic.edu) or Sam S. Yoon (skyoon@korea.ac.kr)
[1]School of Mechanical Engineering, Korea University, Seoul 02841, Republic of Korea
[2]SKKU Advanced Institute of Nanotechnology (SAINT), Sungkyunkwan University (SKKU), Suwon 16419, Republic of Korea
Full list of author information is available at the end of the article

detection capabilities; that is, most of them can only detect two external stimuli, such as pressure and strain[7] or pressure and temperature[8,9]. Although sensors with improved sensing performance capable of detecting three or more external stimuli[10] have recently been developed by incorporating one-dimensional (1D) micro- or nanomaterials in their structures[11], more advanced multifunctional sensors that can simultaneously detect six or more external stimuli have yet to be reported[12,13]. In addition, the sensing accuracy, sensing reliability, and mechanical durability of sensors capable of detecting multiple stimuli remain considerable challenges. The required use of vacuum-based manufacturing techniques along with time-consuming and complex technological steps to enhance the sensing capabilities of materials also limits their subsequent use in commercially viable multifunctional sensors[14,15]. Therefore, in addition to the need to lower the manufacturing cost, a facile, rapid, binder-free, and scalable fabrication process is required to enable such sensors to be used in various practical industrial applications.

Here, we present a flexible multifunctional soft sensor that can detect six external stimuli, including strain (bending), pressure, proximity, temperature, humidity, and UV light. These multifunctional soft sensors are fabricated using the supersonic cold-spraying method with silver nanowires (AgNWs) for improving electrical conductivity, carbon nanotubes (CNTs) as a basic sensing material, zinc oxide (ZnO) for detecting UV light, and PEDOT:PSS as a binder. The supersonic cold-spraying technique used in this study is a simple, rapid, and scalable coating method that does not affect the substrates and has attracted considerable attention as a commercially viable manufacturing method for coating materials with submicrometer-sized particles[16,17]. In particular, the multifunctional soft sensors that have been developed are not only capable of simultaneous detection of multiple stimuli but also possess high selectivity for the abovementioned stimuli. The sensors developed in this work can also scan the topology of a certain object without contacting the object by employing proximity sensing.
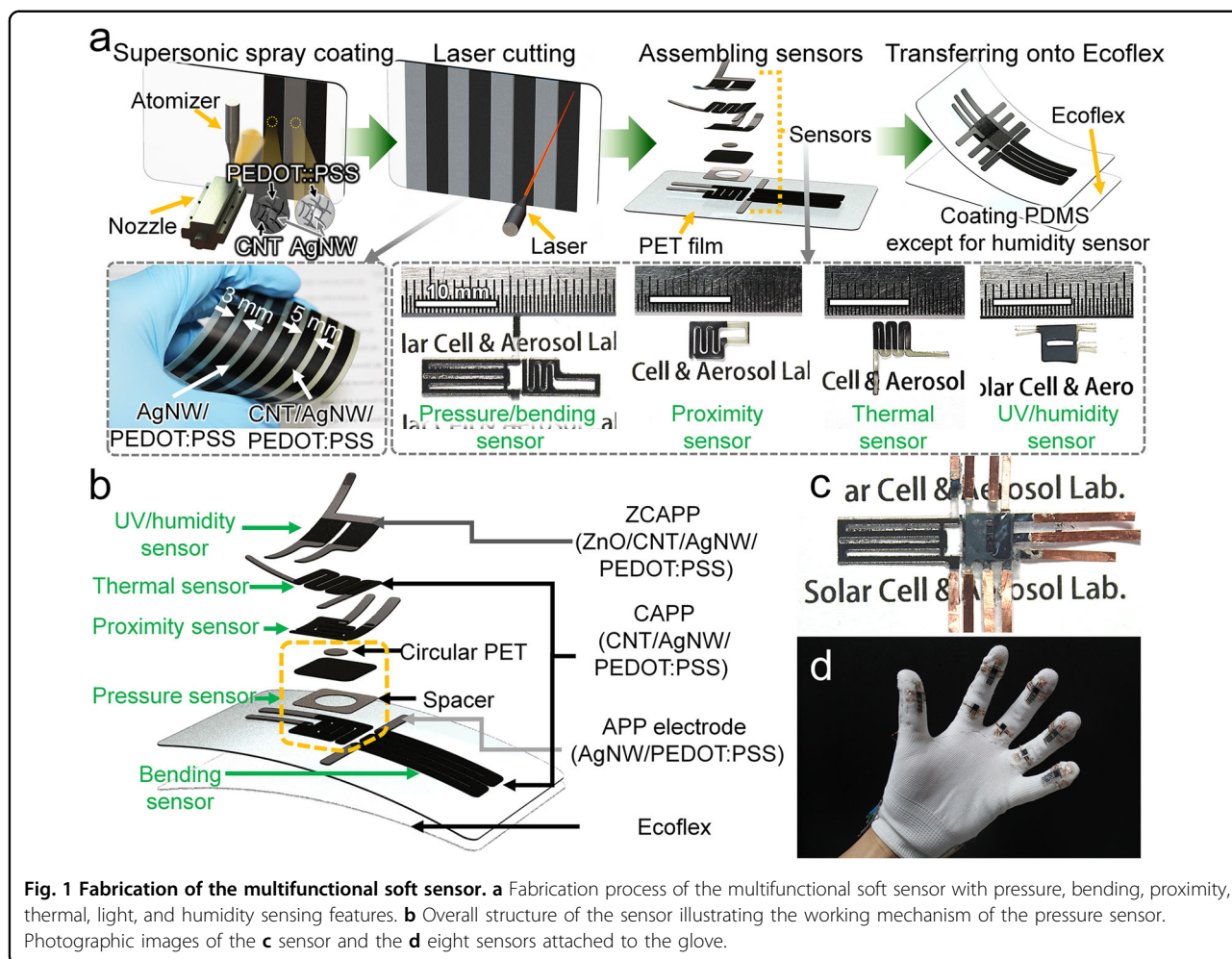
## Results and discussion
### Fabrication of the multifunctional soft sensor

Figure 1a provides a graphical description of the fabrication process (based on the supersonic cold-spraying technique) of the multifunctional soft sensor, which can detect UV light, humidity, temperature, proximity, pressure, and bending (or strain). Initially, the first coating material, namely, the AgNW/PEDOT:PSS (APP) solution, was supersonically sprayed onto a poly(ethylene terephthalate) (PET) film (0.006 mm thick) using a mask (shown as gray stripes on the PET film in Fig. 1a; cf.

Section Materials). The APP solution, which was supplied to the ultrasonic atomizer at a flow rate of 1.5 mL·min$^{-1}$, was atomized into a supersonic air stream during supersonic cold-spraying (the first step in Fig. 1a). The stagnation pressure ($P_0$) and temperature ($T_0$) for forming the supersonic jet were $P_0 = 3$ bar and $T_0 = 150\,°C$, respectively. The number of sweeps of the supersonic nozzle was $N = 3$, with a scan speed of $2\,cm·s^{-1}$. Note that the use of the mask allowed the supersonically sprayed APP solution to be uniformly atomized and thus deposited as stripes (Fig. 1a). Details of the supersonic cold-spraying method can be found elsewhere[16,17]. Next, the second coating material, namely, CNT/AgNW/PEDOT:PSS (CAPP), was supersonically sprayed onto the remaining section of the PET film under the same operating conditions (black stripes on the PET film in Fig. 1a). This coated PET film is referred to as the CAPP/APP film. Note that CNTs were added to the APP solution to enhance the electrical sensitivity of the resulting film (see Section Materials).

During the next step, to equip the sensor with the ability to detect UV light and humidity, the third coating material, namely, ZnO/CNT/AgNW/PEDOT:PSS (ZCAPP), was prepared as a solution (cf. Section Materials). The PET film on which the ZCAPP and APP solutions were deposited is denoted as the ZCAPP/APP film (Fig. 1). The use of ZnO nanoparticles enabled the sensor to respond electrically to variations in humidity and UV light. Next, the CAPP/APP and ZCAPP/APP films were cut into several pieces using a laser cutter (VLS 3.50, Universal Laser Systems, USA), as depicted in Fig. 1b displays the layout of these pieces and the construction of the multifunctional soft sensor. The ZCAPP/APP film was employed for the humidity sensor section. It should be noted that the ZCAPP/APP film was covered by PDMS and also employed in the UV light sensor section; the use of PDMS prevented ZnO from reacting with water molecules. The CAPP/APP films were used for the other sensor sections. Note that the APP strips that formed part of each component served as the electrode that was connected to the copper electrodes that supplied power to the sensor (Fig. 1c). The APP strip was connected to the copper electrode using silver paste (ELCOAT A-200, CANS, Japan). The cut films were sequentially placed on flexible PET and Ecoflex (00-30, SMOOTH-ON, USA) substrates, as depicted in Fig. 1b. The pressure-sensor section incorporated a PET spacer (0.5 mm × 0.5 mm) that was placed between the CAPP and CAPP/APP films, and a circular PET film (0.15 mm in radius) was also inserted above the CAPP film (Fig. 1b). This allowed the external pressure applied to the sensor to be focused at the center of the sensor. Finally, a PDMS coating was used as the top layer of the multifunctional sensor and covered all the sensors except the humidity sensor. The device was dried in an oven for 3 h at 50 °C. A total of eight

**Fig. 1 Fabrication of the multifunctional soft sensor. a** Fabrication process of the multifunctional soft sensor with pressure, bending, proximity, thermal, light, and humidity sensing features. **b** Overall structure of the sensor illustrating the working mechanism of the pressure sensor. Photographic images of the **c** sensor and the **d** eight sensors attached to the glove.
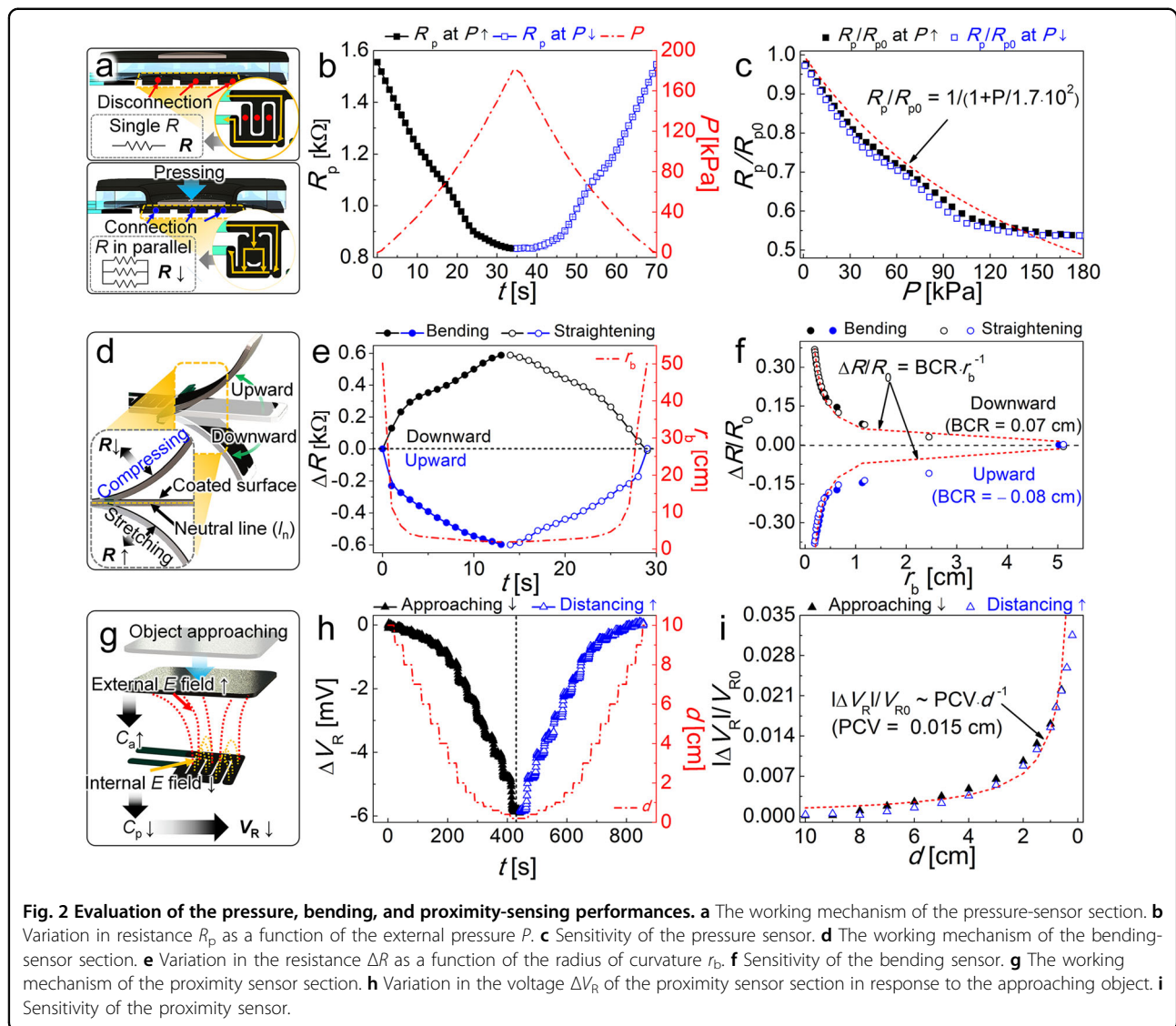
multifunctional sensors were fabricated and attached to a hand glove (Fig. 1d), as described in detail in Section Multifunctional sensing performance when simultaneously monitoring multiple stimuli.

Photographic images of the CAPP/APP and ZCAPP/APP films are presented in Fig. S1a, b, respectively, and Fig. S1c shows the transmittance ($T$) of the APP lines in the 400–800 nm wavelength ($\lambda$) range. The $T$ value of the APP strips at $\lambda = 550$ nm was 86% (Table 1). The sheet resistance ($R_s$) of the APP strips was $R_s = 39$ $\Omega$/sq (Table 1). The high $T$ and low $R_s$ enabled the APP strips to be used as transparent conducting electrodes, not only for the sensor in this study but also for a touch screen in previously reported studies[16]. The SEM images in Fig. S2 show the morphologies of the supersonically deposited APP, CAPP, and ZCAPP coatings on the PET films. In the case of APP, the junctions between the AgNWs were clearly seen to be strongly fused (SEM images in Fig. S2a). This fusion was attributed to the high kinetic energy derived from supersonic cold-spraying, thus yielding an APP film with a low value of $R_s$.

**Table 1 Electrical and optical properties of the films.**

| Film | $R$ ($\Omega$) | $R_s$ ($\Omega \cdot sq^{-1}$) | $T$ (%) |
|---|---|---|---|
| AgNWs/PEDOT:PSS (APP) | 53 | 39 | 86 |
| CNT/AgNWs/PEDOT:PSS (CAPP) | 116 | 82 | – |
| ZnO/CNT/AgNWs/PEDOT:PSS (ZCAPP) | 595 | 312 | – |

The pressure-, bending-, proximity-, and thermal-sensor sections required an electrical resistivity higher than that of the electrode (i.e., the APP strip) (cf. Fig. 1). Hence, the CNT-containing CAPP strips were alternately deposited with the APP strips when fabricating the CAPP/APP film (Fig. 1a). The CNTs were densely deposited between the AgNWs during supersonic cold-spraying (SEM images in Fig. S2b) because the use of an atomizer prevented CNT and AgNW aggregation[17]. This approach made it possible to ensure that the electrical resistivity of the CAPP line was higher ($R = 116$ $\Omega$) than that of the APP strip ($R = 53$ $\Omega$) (Table 1). Similarly to the case of

**Fig. 2 Evaluation of the pressure, bending, and proximity-sensing performances. a** The working mechanism of the pressure-sensor section. **b** Variation in resistance $R_p$ as a function of the external pressure $P$. **c** Sensitivity of the pressure sensor. **d** The working mechanism of the bending-sensor section. **e** Variation in the resistance $\Delta R$ as a function of radius of curvature $r_b$. **f** Sensitivity of the bending sensor. **g** The working mechanism of the proximity sensor section. **h** Variation in the voltage $\Delta V_R$ of the proximity sensor section in response to the approaching object. **i** Sensitivity of the proximity sensor.

CAPP, the ZnO nanoparticles could be uniformly deposited with CNTs and AgNWs by using the atomizer during supersonic cold-spraying (SEM images in Fig. S2c). The electrical resistance of the ZCAPP strip was 595 Ω (Table 1). The presence of ZnO in the ZCAPP/APP film conferred UV light and humidity sensing abilities to the multifunctional soft sensor.

## Pressure, bending, and proximity sensing performance

The pressure-sensor section of the multifunctional soft sensor was composed of CAPP/APP and CAPP films with a circular PET film and PET spacer (surrounded by the yellow dashed line in Fig. 1b). The working principle of the pressure-sensor section was based on measuring the variation in contact resistance between the CAPP/APP and CAPP films with external pressure. Although the CAPP/APP and CAPP films were initially separated by the

spacer, they came into contact with each other, while the circular PET film pushed the CAPP film down to the CAPP/APP film as soon as external pressure was applied.

The application of pressure changed the electrical resistance inside the pressure-sensor section (Fig. 2a). In other words, the CAPP/APP film located at the bottom of the pressure-sensor section (Fig. 1b) was initially designed to serve as a single resistor before pressure was applied (yellow line in the upper image in Fig. 2a). However, it structurally became three resistors as the upper CAPP film came into contact with the CAPP/APP film when external pressure was applied (yellow lines in the lower image in Fig. 2a), thereby lowering the overall resistance of the pressure-sensor section.

On the other hand, because the actual contact materials between the CAPP/APP and CAPP films were AgNWs rather than CNTs, the contact resistance between the two

films can be explained in terms of the contact between two cylindrically shaped AgNWs. The contact resistance ($R_c$) between the two cylinders (i.e., AgNWs in the CAPP/APP and CAPP films) can be expressed as

$$R_c = \frac{\rho}{2a}\left[1 - 1.42\left(\frac{a}{r_{Ag}}\right)\right] \tag{1}$$

where $\rho$ is the resistivity of the AgNWs, $2a$ is the contact length between the two cylinders, and $r_{Ag}$ is the radius of the cylinder, that is, the radius of the AgNW (cf. Fig. S3a). Note that Eq. (1) is valid for $r_{Ag} > a$[18,19]. Through the transformation of Eq. (1) as described in Eqs. (S1) and (S2), Eq. (1) can be transformed to

$$R_c = \frac{\rho}{2a} = \frac{A}{P}, \text{ where } A = \frac{\rho\pi E}{16(1-\nu^2)r_{Ag}} \tag{2}$$

where $\nu$ and $E$ are the Poisson's ratio and Young's modulus of the AgNWs, respectively, and $P$ is the pressure applied to the pressure sensor.

When the CAPP/APP and CAPP films were in contact as a result of external pressure, the resistance $R_c$ and initial resistance of the pressure-sensor section ($R_{p0}$) were connected in parallel (Fig. 2a). Thus, the corresponding resistance of the pressure-sensor section ($R_p$) can be expressed as

$$\frac{1}{R_p} = \frac{1}{R_c} + \frac{1}{R_c} + \frac{1}{R_{p0}}$$
$$R_p = R_{p0}\left(\frac{1}{1+2R_{p0}/R_c}\right) = R_{p0}\left(\frac{1}{1+P/A_2}\right), \text{ where } A_2 = \frac{A}{2R_{p0}} \tag{3}$$

According to Eq. (3), $R_p$ decreases as $P$ increases, which is also observed experimentally (Fig. 2b). As the pressure $P$ is increased from 0 to 180 kPa, the corresponding resistance $R_p$ decreased from 1.55 to 0.83 kΩ. Note that the value of $R_{p0}$ was $R_{p0} = 1.55$ kΩ. The resistance $R_p$ increased again to 1.55 kΩ as $P$ was lowered to 0 kPa. On the other hand, the ratio $R_p/R_{p0}$ was proportional to $1/(1 + P \cdot A_2^{-1})$ [cf. Equation (3)], as also seen in Fig. 2c, indicating that the value of $R_p/R_{p0}$ decreased to 0.537 with increasing $P$. The value of $A_2$ that fits the data in Fig. 2c for both the pressing and releasing stages was $A_2 = 1.71 \times 10^5$ Pa. Fig. S3b illustrates the mechanical durability and electrical stability of the pressure-sensor section of the multifunctional soft sensor. The cyclic pressing/releasing test was conducted for 450 cycles, where $P$ was gradually increased from 20 to 100 kPa every 150 cycles. No discernible degradation in sensor performance was observed during these 450 cycles, and the degree of variation in $\Delta R_p$ was in good correlation with the change in pressure $P$, demonstrating the high reliability and sensitivity of the pressure sensor.

The bending (or strain) sensor section was positioned at the bottom of the multifunctional soft sensor (Fig. 1b). This bending sensor was designed to monitor the motions of human joints, for example, fingers, elbows, and knees, by measuring the variation in electrical resistance resulting from the change in strain. Figure 2d shows the working mechanism of the bending-sensor section depending on whether the bending direction is upward or downward. Note that, in this case, upward bending corresponded to compression of the sensor, whereas downward bending corresponded to stretching because the coated surface of the CAPP film faced upward (Fig. 1b). In other words, the deposited materials (i.e., CNTs, AgNWs, and PEDOT:PSS) comprising the CAPP film were compressed as the film was bent in the upward direction, whereas they were stretched as the film was bent in the downward direction [Fig. 2d and cf. Eqs. (S3–S6)]. It should be emphasized that the electrical resistance of the film decreased as the film was compressed, whereas it increased as the film was stretched.

The electrical resistance ($R$) of the bending-sensor section can be expressed as

$$R = \rho l S^{-1} \tag{4}$$

where $\rho$, $l$, and $S$ are the electrical resistivity (Ω·cm), length (cm), and cross-sectional area (cm$^2$) of the material deposited (i.e., the CAPP film), respectively. Through the logarithmic derivative of Eq. (4), as demonstrated in Eqs. (S7) and (S8), and the expression of strain ($\varepsilon$) via $h$ and $r_b$ in Eqs. (S5) and (S6), where $h$ is the thickness of the strain sensor and $r_b$ is the radius of curvature of the bending-sensor section[20], Eq. (S7) can be rewritten as

$$\frac{dR}{R} = \eta_s\left(\pm\frac{h}{2r_b}\right) \tag{5}$$

where $\eta_s$ is the sensitivity factor or gauge factor (GF).

Upward bending (compression of the deposited materials, cf. Fig. 2d) resulted in the right-hand side of Eq. (5) being negative because the junctions between materials were compressed, thus resulting in a lower value of $R$. On the other hand, the effect of downward bending (stretching of the deposited materials, cf. Fig. 2d) resulted in the right-hand side of Eq. (5) being positive because the junctions were loosened, thereby causing the resistance $R$ to increase.

In the bending test, $r_b$ was initially set as 50.2 mm. As the sensor was bent upward, $r_b$ decreased to 1.9 mm (red dash-dotted curve in Fig. 2e), which resulted in a decrease in electrical resistance ($\Delta R < 0$) because of the compression of the deposited materials (blue solid curve with filled circles in Fig. 2e). As the bent sensor was returned to its initial configuration ($r_b = 50.2$ mm), the value of $\Delta R$

returned to zero (blue solid curve with open circles in Fig. 2e). Conversely, as the sensor was bent downward with $r_b = 1.9$ mm, the value of $\Delta R$ was positive because the deposited materials were stretched (black solid curve with filled circles in Fig. 2e). As the bent sensor was released to return to its initial configuration ($r_b = 50.2$ mm), the value of $\Delta R$ returned to zero (black solid curve with open circles in Fig. 2e). Regardless of the bending direction, the corresponding maximum absolute value of $\Delta R$ of the sensor in the bent state was always equal to 0.6 k$\Omega$, verifying its structural reliability and superiority as a bending sensor.

In addition, the change in the ratio $\Delta R/R_0$ (where $R_0 = 1.58\ \Omega$) was also explored by varying $r_b$ (Fig. 2f). During both downward and upward bending, as the radius of curvature $r_b$ was decreased from 50.2 mm to 1.9 mm, the corresponding absolute value of the ratio $\Delta R/R_0$ increased; notably, the increasing trends of the two cases were almost identical. As a result, the values of the bending coefficient of resistance (BCR, defined as BCR $= \Delta R/R_0 \cdot r_b$) for downward and upward bending were similar (Fig. 2f). In addition to the bendability, the cyclability of the sensor was also explored (Fig. S3c) by holding $r_b$ constant at 1.9 mm and conducting 500 bending cycles. The value of $\Delta R$ remained at 0.63 k$\Omega$ after 500 cycles without significant degradation.

Figure 2g illustrates the working mechanism of the proximity sensor section, which is based on the fringe capacitance (i.e., the capacitance increases when an object is approaching). In other words, the proximity sensor section was designed to respond to an approaching object by employing the fact that the electric field strength ($E$) in the space between the electrodes in the CAPP/APP film (Fig. 1) was affected by the movement of the object (i.e., a metal plate of 10 cm × 10 cm; cf. Fig. 2g). Specifically, the CAPP/APP film of the proximity sensor section was connected to an external circuit composed of a 2.2 M$\Omega$ resistor and a bridge rectifier with an AC voltage of 5 V and a frequency of 100 kHz applied by an external multifunction generator (Fig. S3d). Note that the direct measurement of voltage from the proximity sensor section could produce electrical noise because of the fine vibration of the wire as the sensor moved. Accordingly, to reduce this noise, the output DC voltage from the resistor connected to the external circuit was measured by employing a bridge rectifier to convert the AC signal to a DC signal (Fig. S3d).

The initial capacitance of the proximity sensor section between the two electrodes ($C_{p0}$), which is defined in Eq. (S9), was constant. However, when an object was approaching the sensor, this induced capacitance between the sensor and object ($C_a$) and ultimately affected the capacitance of the sensor ($C_p$), as demonstrated in Fig. S3e and Eq. (S10). That is, $C_p$ varied as the distance between the sensor and object ($d$) changed [cf. Eq. (S11)]. In particular, $C_a$ was inversely proportional to $d$ (Fig. S3e). Because the change in $C_p$ resulted from the variation in $d$, the applied voltages of the proximity sensor section and resistor connected in series with the sensor also varied. The total voltage ($V_t$) added to the voltage of the proximity sensor ($V_p$) and that of the resistor ($V_R$) was constant at 5 V. The impedance of the proximity sensor ($X_c$) is proportional to $1/C_p$, and thus, the current of the proximity sensor and resistor ($I$) is $V_t/(1/\omega C_p + R)$, where $\omega$ is the frequency. Therefore, $V_R$ can be calculated as follows

$$V_R = V_t - V_p = V_t - IX_c = \frac{V_t R}{1/\omega C_p + R} \tag{6}$$

Substituting $C_p$ for $c_1 - c_2/d$, where $c_1$ and $c_2$ are the effective constants in Eq. (S11) yields the following expression

$$V_R = \frac{V_t R}{1/\omega(c_1 - c_2/d) + R} \tag{7}$$

In the above equation, as $d$ decreases, the term $1/\omega(c_1 - c_2/d)$ increases, and thus, $V_R$ decreases.

Figure 2h shows the voltage variation ($\Delta V_R = V_R - V_{R0}$) as $d$ is varied from 10 to 0.2 cm and again from 0.2 to 10 cm. As $d$ was decreased, $\Delta V_R$ increased. For example, as $d$ was decreased from 10 to 5 cm, $\Delta V_R$ slowly decreased from 0 to $-2.98$ mV. However, $\Delta V_R$ rapidly decreased from $-2.93$ to $-5.8$ mV when $d$ was decreased from 5 to 0.2 cm. Similarly, $\Delta V_R$ dramatically increased from $-5.8$ to $-2.91$ mV when $d$ was increased from 0.2 to 5 cm.
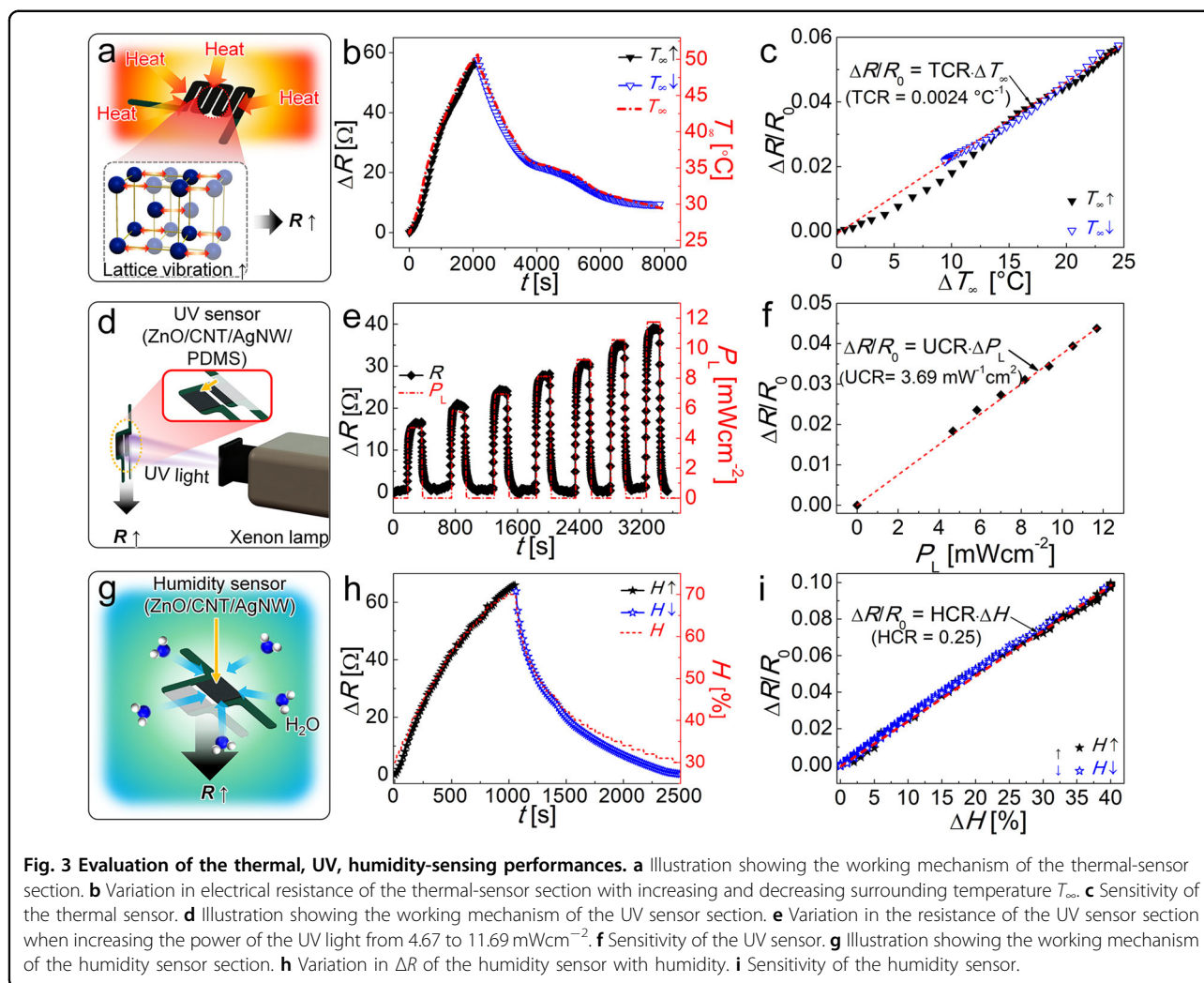
The propensity for the rapid increase in voltage with decreasing $d$ can be explained as follows. Because $V_t$ is constant, $\Delta V_R$ can be expressed as

$$\Delta V_R = \Delta V_t - \Delta V_p = -\Delta V_p \tag{8}$$

When an object approached the proximity sensor section, which was indicated by a decrease in $d$, $C_p$ decreased from $C_{p1} + C_{p2}$ to $C_{p1} + C_{p2} - C_a$, as demonstrated in Eqs. (S9) and (S10). Therefore, $\Delta V_R$ can be simplified as shown in Eq. (S13), which indicates that the magnitude of $\Delta V_R$ increases as $d$ decreases. Accordingly, the proximity coefficient of the voltage (PCV) can be defined by the following relation between $|\Delta V_R|/V_R$ and $d$

$$\frac{|\Delta V_R|}{V_{R0}} \sim \frac{\text{PCV}}{d} \tag{9}$$

As presented in Fig. 2i, the value of $|\Delta V_R|/V_R$ dramatically increased from 0 to 0.035 as an object approached (i.e., $d$ decreased). Accordingly, the variation of $|\Delta V_R|/V_R$ largely corresponded to that of PCV/$d$ when PCV = 0.015. To estimate the stability of the proximity sensor,

**Fig. 3 Evaluation of the thermal, UV, humidity-sensing performances. a** Illustration showing the working mechanism of the thermal-sensor section. **b** Variation in electrical resistance of the thermal-sensor section with increasing and decreasing surrounding temperature $T_\infty$. **c** Sensitivity of the thermal sensor. **d** Illustration showing the working mechanism of the UV sensor section. **e** Variation in the resistance of the UV sensor section when increasing the power of the UV light from 4.67 to 11.69 mWcm$^{-2}$. **f** Sensitivity of the UV sensor. **g** Illustration showing the working mechanism of the humidity sensor section. **h** Variation in $\Delta R$ of the humidity sensor with humidity. **i** Sensitivity of the humidity sensor.

the voltage variation in the proximity sensor section was measured by shortening $d$ to 7, 2.5, and 0.2 cm for 30 cycles (1800 s) (Fig. S3f). The variation in the voltage of the proximity sensor ($\Delta V_R$) increased to 0.0005, 0.0025, and 0.006 V as $d$ was decreased to 7, 2.5, and 0.2 cm, respectively; notably, the value of $\Delta V_R$ remained essentially the same for each value of $d$.

### Thermal, UV, and humidity sensing performance

Thermal sensors are used to measure changes in the surrounding temperature. They can be subdivided into two types depending on their specific working mechanism: contact and noncontact sensors[21]. A thermal sensor of the contact type, such as a thermocouple, a resistance-temperature detector (RTD), and a thermistor, can detect the surrounding temperature by measuring the change in electrical resistance or thermal electromotive force. In contrast, noncontact thermal sensors, such as infrared thermometers, can detect the temperature of an object by measuring the radiant energy it emits. Among these two types of

thermal sensors, the contact type is considered to be more suitable for a miniaturized thermal sensor because it does not require any additional components that are necessary for the noncontact type, for example, an optical system or a detector[22]. Considering this advantage of contact-type sensors, the working mechanism of such a sensor was employed in the thermal-sensor section in this study. Specifically, the ability to detect the change in temperature of an object by measuring the change in electrical resistance was the focus.

In this study, CNTs were attached to AgNWs (cf. Fig. S2), which meant that the change in electrical resistance of the thermal-sensor section was similar to that of ordinary metals. In other words, as the metallic material was heated, the vibration of its lattice (phonons), which originates from the oscillation of atoms, increased (Fig. 3a). This resulted in a decrease in the mobility of atoms because of the increased possibility of 'collisions' between adjacent atoms. That is, for metallic materials, the resistance increased with increasing temperature[23], which was also observed for the thermal sensor developed in this study.

The thermal sensing performance was evaluated by measuring the variation in resistance ($\Delta R$) of the thermal-sensor section as the ambient temperature ($T_\infty$) was increased from 26 to 50 °C in a thermostatic chamber. Figure 3b shows the correlation between $\Delta R$ and $T_\infty$. As $T_\infty$ increased from 25 to 50 °C (i.e., during the time interval of $0 < t < 2000$ s), the corresponding value of $\Delta R$ increased from 0 to 56 Ω. Subsequently, as $T_\infty$ was decreased from 50 to 29.4 °C, the value of $\Delta R$ decreased from 57.3 to 9.5 Ω. In particular, the change in $\Delta R$ was clearly observed to be correlated with that of $T_\infty$. In addition, the sensitivity of the thermal-sensor section was evaluated using the temperature coefficient resistance (TCR)

$$\text{TCR} = \frac{R - R_0}{R_0} \frac{1}{T_\infty - T_{\infty 0}} = \frac{\Delta R}{R_0} \frac{1}{\Delta T_\infty} \quad (10)$$

where the initial resistance ($R_0$) and ambient temperature ($T_{\infty 0}$) were 1.014 kΩ and 25 °C, respectively. As $\Delta T_\infty$ was changed, the value of $\Delta R/R_0$ changed linearly, while the TCR, which is the slope of the dependence of $\Delta R/R_0$ on $\Delta T_\infty$, was nearly constant at 0.0024 °C$^{-1}$ (Fig. 3c).

The multifunctional sensor developed in this study was also capable of detecting UV light (Fig. 1b). Because UV light can cause severe damage to human skin, detecting UV light is one of the important functions required for e-skin. UV light sensors can be classified into three types based on their working principle: photovoltaic[24], photoconductive[25], and photoelectron-emitting sensors[26]. Among them, the photoconductive type was employed for the UV light sensor section in this study. When semiconductive materials are exposed to UV light, their electrical conductivity changes as the electrons in the valence band are excited to the conduction band. Considering this phenomenon, the semiconductive material ZnO was employed as the material in the UV sensor section[27]. The working mechanism of the UV sensor was based on the absorption and desorption of dioxygen ($O^2$) at the surface of ZnO[28]. When ZnO was irradiated with UV light, the formation of electron ($e^-$)–hole ($h^+$) pairs (exciton) was induced, lowering the electron concentration in the conduction band (i.e., $O^2 + (e^- + h^+) \rightarrow O^{2-} + (h^+)]$[29] and leading to an increase in electrical resistance. In contrast, when the UV light was switched off, $O^2$ desorbed from the surface of ZnO [that is, $O^{2-} + (h^+) \rightarrow O^2 + (e^- + h^+)$], increasing the electron concentration in the conduction band, and thus, decreasing the resistance[30,31].

ZnO nanoparticles with an average size of 50 nm were hybridized with CNTs and AgNWs by using the supersonic cold-spraying method (cf. Section Materials) to fabricate the ZCAPP/APP film. As illustrated in Fig. 3d, the variation in electrical resistance ($\Delta R$) of the UV sensor section was measured at a varyin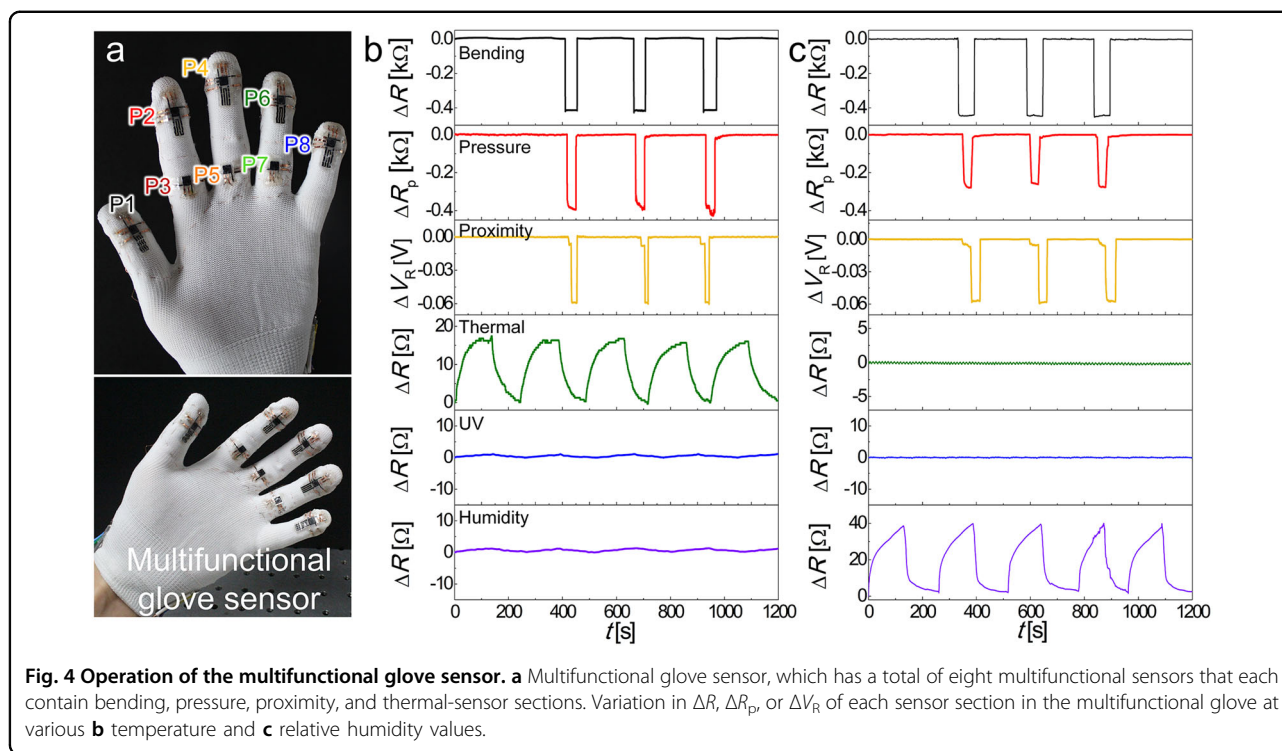g power density of UV light ($P_L$) from 4.67 to 11.69 mW cm$^{-2}$ using a xenon lamp and a shortpass filter (cf. Section Characterization). Figure 3e shows the change in $\Delta R$ from 4.67 to 11.69 mW cm$^{-2}$ with a stepwise $P_L$ increase of 1.17 mW cm$^{-2}$. Note that the initial resistance of the UV sensor ($R_0$) before UV irradiation was 895.2 Ω. The value of $\Delta R$ increased from 0 to 16.4 Ω as $P_L$ was increased to 4.67 mW cm$^{-2}$. When the UV light was turned off, the corresponding value of $\Delta R$ returned to its initial value. As $P_L$ was increased to 5.84, 7.01, 8.18, 9.35, 10.52, and 11.69 mW cm$^{-2}$, the corresponding maximum values of $\Delta R$ also gradually increased to 915.7, 919.1, 922.4, 925.6, 930.1, and 934.2 Ω, respectively.

The sensitivity of the UV sensor was more carefully characterized by additionally examining the degree of change in the ratio $\Delta R/R_0$ of the UV sensor with increasing $P_L$ (Fig. 3f). As $P_L$ was increased from 4.67 to 11.69 mW cm$^{-2}$, the ratio $\Delta R/R_0$ linearly increased up to 0.045. Thus, the UV light coefficient of the resistance (UCR) had a constant value of 3.69 mW$^{-1}$ cm$^2$. Figure S4a shows the stable performance of the UV sensor by measuring $\Delta R$ for 70 cycles when $P_L = 7.01$ mW cm$^{-2}$. During cycling, $\Delta R$ was observed to remain constant at 25 Ω, confirming the outstanding stability of the UV light sensor.

The humidity sensing performance was also explored, as shown in Fig. 3g–i. Humidity sensors generally operate by exploiting the variations in capacitance[32] or electrical conductivity/resistivity[33] in response to changes in humidity. For example, $H_2O$ molecules serve as electron donors in the presence of moisture when they are adsorbed on the surface of CNTs. This results in a decrease in the hole concentration, thereby increasing the electrical resistivity of the CNTs[34,35]. Therefore, the adsorption of $H_2O$ molecules, which is associated with the humidity level, leads to an increase in the resistance of CNTs[36]. In contrast to CNTs, the electrical resistance of ZnO, which is an n-type semiconductor, decreases as $H_2O$ molecules are adsorbed[37,38].

Specifically, in the composite comprised of CNTs and ZnO, the change in electrical resistance depends on the feature of the material that is quantitatively dominant[39,40]. In the present study, the change in resistance of the humidity sensor section was dictated by the features of the CNTs rather than those of ZnO (cf. Fig. 3g). The variation in the electrical resistance of the humidity sensor section was measured by varying the humidity level in the chamber, in which the humidity value was recorded using a data logger (LR8400-20, HIOKI, Japan) and humidity sensor (Z2000, HIOKI, Japan).

Figure 3h illustrates the variation in electrical resistance ($\Delta R$) of the humidity sensor section with changes in the value of the relative humidity ($H$). The initial relative humidity ($H_0$) was maintained at 30%. As $H$ was increased from 30% to 70%, the value of $\Delta R$ also increased from 0 to

**Fig. 4 Operation of the multifunctional glove sensor. a** Multifunctional glove sensor, which has a total of eight multifunctional sensors that each contain bending, pressure, proximity, and thermal-sensor sections. Variation in $\Delta R$, $\Delta R_p$, or $\Delta V_R$ of each sensor section in the multifunctional glove at various **b** temperature and **c** relative humidity values.

66 Ω (solid curve with black stars in Fig. 3h). As $H$ gradually decreased from 70% to 30%, the value of $\Delta R$ also decreased to its initial value of 0 Ω (solid curve with blue stars in Fig. 3h). The change in the curve of $\Delta R$ correlated with that of $H$. The sensitivity of the humidity sensor section was evaluated by exploring the change in the ratio $\Delta R/R_0$ as the relative humidity $\Delta H$ was increased. The humidity coefficient of the resistance (HCR) remained constant at 0.25 when $\Delta H$ was increased from 0 to 40% (Fig. 3i). The HCR, which indicates the sensitivity of the humidity sensor, remained constant when the relative humidity was either increased or decreased, demonstrating the characteristics required for a humidity sensor. Figure S4b shows the results of the stability test of the humidity sensor, with the sensor undergoing 100 cycles at different values of $H$. In all cases, no discernible degradation in performance was observed, demonstrating the excellent performance of the humidity sensor.

**Multifunctional sensing performance when simultaneously monitoring multiple stimuli**

It should be emphasized that each sensor section in the multifunctional sensor device should selectively and accurately respond to its corresponding signal without interference from the other sensor sections. In this study, the multilayered structure selected for the design of the multifunctional sensor made it possible to distinguish and detect different signals without such interference (cf. Fig. 1b). To evaluate whether the multifunctional sensor could

selectively monitor different stimuli in practical situations, a multifunctional glove was equipped with the sensor, and the aim was to use it as an e-skin (Fig. 4a). Four sensor sections, namely, those measuring the bending strain, pressure, proximity, and temperature, were installed closer to the fingertips at points P1, P2, P4, P6, and P8 on the glove, whereas three sensor sections (those measuring the pressure, proximity, and temperature) were installed at other points (P3, P5, and P7) farther from the fingertip, where the finger could not be bent and thus, the bending-sensor section was unnecessary (Fig. 4a).
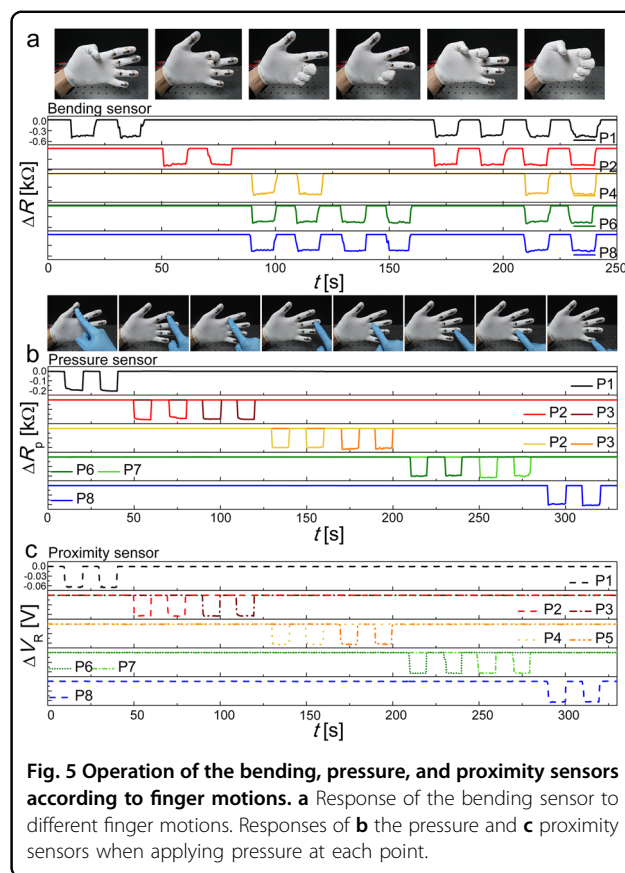
First, the signals from each sensor section were monitored at different temperatures while alternately placing the glove inside the thermal chamber and removing it again (Fig. 4b). The temperature inside the chamber was 40 °C. The first and second cycles of thermal sensing (green solid curve in Fig. 4b) resulted in an increase in the electrical resistance variation $\Delta R$ from 0 to 17 Ω when the glove sensor was inside the chamber. Then, the value of $\Delta R$ returned to 0 Ω as the glove sensor was removed from the chamber. In particular, during thermal sensing, the other sensor sections, that is, the bending, pressure, and proximity sensors, did not produce any signals (Fig. S5a), demonstrating the excellent operating performance of the thermal-sensor section without any interference from the other sensor sections.

In addition, the index finger was bent a few times in the direction of the thumb when the glove sensor was located inside the chamber. The value of $\Delta R$ of the bending-

sensor section decreased to −0.4 kΩ when the index finger was bent (black solid line in Fig. 4b). Similarly, the proximity sensor section also responded well when the index finger and thumb approached each other, resulting in the value of $\Delta V_R$ being changed from 0 to −0.06 V. As the two fingers touched each other, the value of $\Delta R$ associated with the pressure-sensor section decreased from 0 to −0.4 kΩ. No changes were observed in the values of ΔR associated with the UV and humidity sensor sections. These results confirmed that each sensor section in the multifunctional glove sensor was capable of selectively monitoring the corresponding stimuli without interference from other sensor sections.
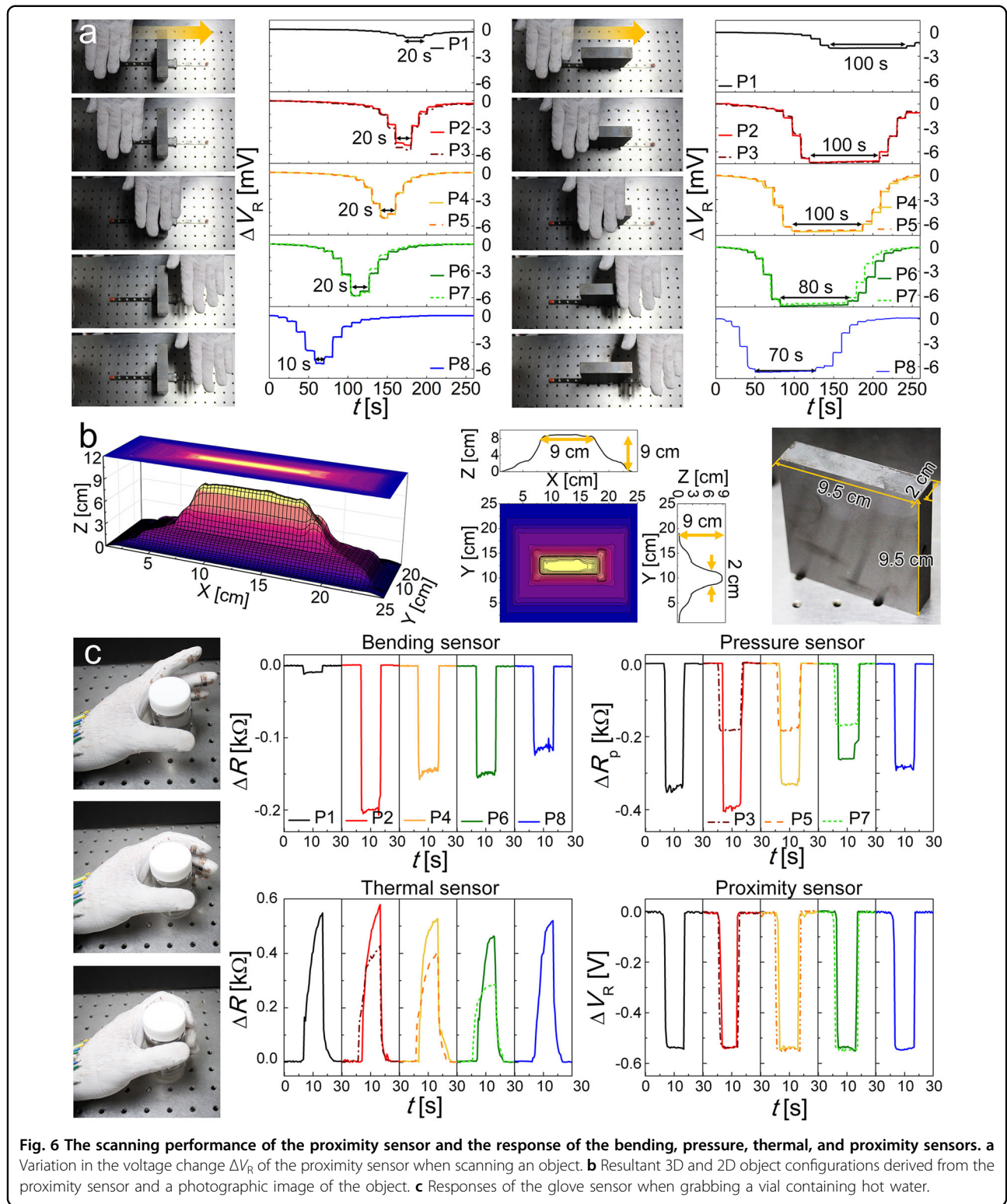
In addition, to evaluate the humidity sensing performance, the glove sensor was alternately placed inside a humidity chamber with an interior relative humidity of 70% and then removed again (Fig. 4c). As shown in Fig. 4c, the $\Delta R$ of the humidity sensor section increased from 0 to 40 Ω when the glove sensor was placed in the chamber, after which the $\Delta R$ returned to 0 Ω when the sensor was removed from the chamber (purple solid line in Fig. 4c). Similar to the case shown in Fig. 4b, during finger movement in the humidity chamber, the bending, pressure, and proximity sensor sections also performed well without interference from the other sensor sections (Fig. 4c). For example, when the index finger was bent and approached the thumb, the $\Delta R$ of the bending-sensor section decreased from 0 to −0.4 kΩ, and the $\Delta R$ of the proximity sensor section also decreased from 0 to −0.0067 V. Note that because the temperature and UV light did not change in this case, the thermal and UV light sensor sections did not produce any signals (Fig. S5b). Additionally, contact between the two fingers resulted in a decrease in the $\Delta R_p$ of the pressure-sensor section from 0 to −0.28 kΩ. These results additionally confirmed that the multifunctional glove sensor could selectively distinguish between different stimuli without interference.

To more precisely evaluate the bending, pressure, and proximity sensing performance of the glove sensor, further experiments were conducted, as shown in Fig. 5. First, whenever the fingers were bent, the bending-sensor section corresponding to each finger responded properly (Fig. 5a). Second, whenever each sensor on the glove was touched by another finger, the pressure and proximity sensor sections corresponding to each touch also exhibited a proper response (Fig. 5b and c). In addition, the shape of an object can be identified by noncontact scanning using a glove sensor (Fig. 6a and b). The hand wearing the glove was moved across an object in the horizontal direction at a scan speed of 0.1 cm/s. The glove was held 6 cm above the object in the vertical direction. As the glove sensor moved in the horizontal direction near the object (a parallelepiped), the proximity sensors at each finger started to respond by detecting a variation in



**Fig. 5 Operation of the bending, pressure, and proximity sensors according to finger motions. a** Response of the bending sensor to different finger motions. Responses of **b** the pressure and **c** proximity sensors when applying pressure at each point.

the voltage change $\Delta V_R$ (Fig. 6a). In particular, different variation times in the $\Delta V_R$ were observed depending on the orientation of the object, that is, 10–20 s when the object was parallel to the glove sensor or 70–100 s when the object was perpendicular to the sensor. Note also that the variation at point P1 was the lowest because the distance between P1 and the object was the longest. The configuration of the object could be derived based on the performance of the glove sensor (Fig. 6b).

The bending, pressure, thermal, and proximity sensors were also tested (Fig. 6c) by grabbing a vial containing hot water at 60 °C with the glove sensor. The index finger experienced the highest degree of bending when clasping the vial, with the degree of bending decreasing in the following order: middle, ring, and little fingers, and then the thumb. This result is clearly observed from the extent of variation in the resistance change $\Delta R$ of the bending-sensor section. Similarly, the magnitude of $\Delta R$ corresponding to the pressure-sensor section reflected the pressure applied by each finger when holding the vial. The thermal-sensor section also responded to the pressure because an increase in temperature depended on the contact surface area subjected to the pressure. The proximity sensor sections also responded properly when the vial was being grabbed and held. Compared to the

**Fig. 6 The scanning performance of the proximity sensor and the response of the bending, pressure, thermal, and proximity sensors. a** Variation in the voltage change $\Delta V_R$ of the proximity sensor when scanning an object. **b** Resultant 3D and 2D object configurations derived from the proximity sensor and a photographic image of the object. **c** Responses of the glove sensor when grabbing a vial containing hot water.

other sensors, the response of the proximity sensor at all points was constant because the dielectric constant and the distance to the object did not change with a change in pressure.

## Conclusion

We presented a high-performance multifunctional soft sensor capable of sensing six stimuli: pressure, bending, temperature, proximity, UV light, and humidity. The

multifunctional sensor was fabricated by employing the nonvacuum, single-step supersonic cold-spraying technique. The high performance of the sensor was attributed to the fabrication approach, namely, the incorporation of an ultrasonic atomizer to the supersonic cold-spraying technique. This allowed the formation of materials comprising submicrometer-sized particles, that is, silver nanowires (AgNWs), carbon nanotubes (CNTs), and zinc oxide (ZnO), along with the conducting polymer PEDOT:PSS as a binder (used to increase the adhesion to the substrate without significantly increasing resistance); moreover, all of these materials were uniformly and densely deposited on a flexible substrate. Furthermore, deposition of the supersonically sprayed films as a multilayered structure facilitated simultaneous sensing of six stimuli without interference among the different functions. Additionally, the multifunctional glove sensor, which holds high potential for use as an e-skin, demonstrated contactless three-dimensional (3D) scanning performance along with the simultaneous ability to sense changes in pressure, bending strain, temperature, UV light, and humidity.

## Experimental methods

### Materials

The electrodes of the developed sensors were fabricated using silver nanowires (AgNWs) with a diameter of 20 nm and a length of 10 μm and poly(3,4-ethylenedioxythiophene)-poly(styrene sulfonate) (PEDOT:PSS). The 0.15 wt% AgNW precursor dispersed in isopropyl alcohol (IPA) was obtained from Aiden (Republic of Korea), and PEDOT:PSS was purchased from Sigma−Aldrich (USA). The PEDOT:PSS solution was prepared by dissolving 0.1 g of PEDOT:PSS in 100 mL of deionized (DI) water. The AgNW/PEDOT:PSS solution was prepared by mixing the AgNW precursor, PEDOT:PSS solution, and IPA (Duksan, Republic of Korea) at a weight ratio of 1:2:3.

The MWCNT/AgNW/PEDOT:PSS solution was prepared by blending 0.03 g of multiwalled carbon nanotubes (Sigma−Aldrich, USA) with a diameter of 50–90 nm with 60 mL of the AgNW/PEDOT:PSS solution. The zinc oxide (ZnO)/CNT/AgNW/PEDOT:PSS solution was prepared by mixing 0.015 g of ZnO nanoparticles with a diameter of 50 nm (Sigma−Aldrich, USA), 0.015 g of CNTs, and 60 mL of the AgNW/PEDO:PSS solution.

### Characterization

The surface morphologies of the fabricated films were characterized using scanning electron microscopy (SEM, S-5000, Hitachi, Japan). The sheet resistance ($R_s$) of the films was measured by a sheet resistance meter (FPP-400, Dasol Eng., Republic of Korea). The variations in the resistance ($R$) and DC voltage ($V_{dc}$) of the sensor were recorded using a digital multimeter (GDM-8261, GW Instek, Taiwan) equipped with two probes. The pressure ($P$) applied to the sensor was measured using a force gauge (FG-6020SD, LUTRON ELECTRONIC, USA). The AC voltage ($V_{ac}$) was supplied to the sensor by a multifunction generator (WF1973, NF Corporation, Japan). The ambient temperature ($T_\infty$) of the thermostatic chamber (DZF-6020, GYYUHUA, China) was measured using a data recorder (MV 1000, YOKOGAWA, Japan) with a thermocouple (K-type). The power density of the UV light ($P_L$) was controlled using a light source (66902, output beam size of 33 mm, Oriel Instruments, USA) equipped with a light power meter (1919-R, Newport, USA), a photodiode sensor (918D-UV-OD3R, Newport, USA), and a shortpass filter (10SWF-400-B, Newport, USA). The humidity in the experimental chamber was measured using a data recorder (LR8400-20, HIOKI, Japan) with a humidity sensor (Z2000, HIOKI, Japan). The bending test and the corresponding cycling test were carried out using a horizontal motorized test stand (COAD 772, OCEAN SCIENCE, Republic of Korea).

### Author details
[1]School of Mechanical Engineering, Korea University, Seoul 02841, Republic of Korea. [2]SKKU Advanced Institute of Nanotechnology (SAINT), Sungkyunkwan University (SKKU), Suwon 16419, Republic of Korea. [3]Department of Mechanical and Manufacturing Engineering, University of Calgary, 2500 University Dr. NW, Calgary, AB T2N 1N4, Canada. [4]Department of Nano Engineering, Sungkyunkwan University (SKKU), Suwon 16419, Republic of Korea. [5]Department of Chemistry, College of Science, King Saud University, Riyadh 11451, Saudi Arabia. [6]Department of Mechanical and Industrial Engineering, University of Illinois at Chicago, 842 W. Taylor Street, Chicago, IL 60607-7022, USA

### Author contributions
The research concept was proposed by H.J. and S.S.Y. The fabrication of sensors and data collection/analysis were conducted by H.S.J. and C.-W.P., and SEM analysis was carried out by A.A. The paper was written and edited by H.S.J. and S.A. and reviewed by M.E.-N., A.L.Y., and S.S.Y. All authors read and approved the paper.

### Competing interests
The authors declare no competing interests.

## References

1. Maynard, A. D. Navigating the fourth industrial revolution. *Nat. Nanotechnol.* **10**, 1005 (2015).
2. Ezechina, M., Okwara, K. & Ugboaja, C. The Internet of Things (Iot): a scalable approach to connecting everything. *Int. J. Eng. Sci.* **4**, 09–12 (2015).
3. Ge, J. et al. A bimodal soft electronic skin for tactile and touchless interaction in real time. *Nat. Commun.* **10**, 1–10 (2019).
4. Rus, D. & Tolley, M. T. Design, fabrication and control of soft robots. *Nature* **521**, 467 (2015).
5. Roland, T., Wimberger, K., Amsuess, S., Russold, M. F. & Baumgartner, W. An insulated flexible sensor for stable electromyography detection: application to prosthesis control. *Sensors* **19**, 961 (2019).
6. Lin, Z. et al. Triboelectric nanogenerator enabled body sensor network for self-powered human heart-rate monitoring. *ACS Nano* **11**, 8830–8837 (2017).
7. Boutry, C. M. et al. A stretchable and biodegradable strain and pressure sensor for orthopaedic application. *Nat. Electron* **1**, 314 (2018).
8. An, B. W., Heo, S., Ji, S., Bien, F. & Park, J-U. Transparent and flexible fingerprint sensor array with multiplexed detection of tactile pressure and skin temperature. *Nat. Commun.* **9**, 2458 (2018).
9. Han, S. et al. Thermoelectric polymer aerogels for pressure–temperature sensing applications. *Adv. Funct. Mater.* **27**, 1703549 (2017).
10. Liao, X. et al. A highly stretchable ZnO@ fiber-based multifunctional nanosensor for strain/temperature/UV detection. *Adv. Funct. Mater.* **26**, 3074–3081 (2016).
11. Ding, L. et al. Ultrasensitive multifunctional magnetoresistive strain sensor based on hair-like magnetization-induced pillar forests. *Adv. Electron Mater.* **6**, 1900653 (2019).
12. Hua, Q. et al. Skin-inspired highly stretchable and conformable matrix networks for multifunctional sensing. *Nat. Commun.* **9**, 244 (2018).
13. Zhang, F., Zang, Y., Huang, D., Di, C.-A. & Zhu, D. Flexible and self-powered temperature–pressure dual-parameter sensors using microstructure-frame-supported organic thermoelectric materials. *Nat. Commun.* **6**, 8356 (2015).
14. Wang, S. et al. Skin electronics from scalable fabrication of an intrinsically stretchable transistor array. *Nature* **555**, 83–88 (2018).
15. Son, D. et al. Multifunctional wearable devices for diagnosis and therapy of movement disorders. *Nat. Nanotechnol.* **9**, 397–404 (2014).
16. Lee, J. G. et al. Production of flexible transparent conducting films of self-fused nanowires via one-step supersonic spraying. *Adv. Funct. Mater.* **27**, 1602548 (2017).
17. An, S., Joshi, B., Yarin, A. L., Swihart, M. T. & Yoon, S. S. Supersonic cold spraying for energy and environmental applications: one-step scalable coating technology for advanced micro-and nanotextured materials. *Adv. Mater.* **32**, 1905028 (2020).
18. Holm R. *Electric Contacts: Theory and Application* (Springer Science & Business Media, 2013).
19. Timsit S. Electrical contact resistance: properties of stationary interfaces. Electrical Contacts-1998. in *Proc. Forty-Fourth IEEE Holm Conference on Electrical Contacts (Cat. No. 98CB36238)* 1—19 (IEEE; 1998).
20. Pelot, D., Jun, S. & Yarin, A. Bentonite dispersions: transition from liquid-like to solid-like behavior and cracking. *J. Non Newton. Fluid Mech.* **219**, 50–64 (2015).
21. Jiang, G. et al. Luminescent La2O2S: Eu3+ nanoparticles as non-contact optical temperature sensor in physiological temperature range. *Mater. Lett.* **143**, 98–100 (2015).
22. Moser, Y. & Gijs, M. A. Miniaturized flexible temperature sensor. *J. Microelectromech Syst.* **16**, 1349–1354 (2007).
23. Larrimore, L. M. *Low Temperature Resistivity.* (Swarthmore College Computer Society; 2005).
24. Zheng, W. et al. Vacuum-ultraviolet photovoltaic detector. *ACS Nano* **12**, 425–431 (2018).
25. Cao, R. et al. Black phosphorous photodetectors: black phosphorous/Indium selenide photoconductive detector for visible and near-infrared light with high sensitivity (Advanced Optical Materials 12/2019). *Adv. Opt. Mater.* **7**, 1970047 (2019).
26. Li, T. et al. Local stress enhanced photocurrent of visible light photo-detection in Cs2AgBiBr6 single crystal. *Appl. Phys. Lett.* **115**, 131103 (2019).
27. Harikrishnan, G. et al. Negative photoresponse in ZnO–PEDOT: PSS nanocomposites and photogating effects. *Nanoscale Adv.* **1**, 2435–2443 (2019).
28. Boscarino, S. et al. Investigation of ZnO-decorated CNTs for UV light detection applications. *Nanomater* **9**, 1099 (2019).
29. Fan, S.-W., Srivastava, A. K. & Dravid, V. P. UV-activated room-temperature gas sensing mechanism of polycrystalline ZnO. *Appl. Phys. Lett.* **95**, 142106 (2009).
30. Fan, S.-W., Srivastava, A. K. & Dravid, V. P. Nanopatterned polycrystalline ZnO for room temperature gas sensing. *Sens. Actuators, B* **144**, 159–163 (2010).
31. Melnick, D. A. Zinc oxide photoconduction, an oxygen adsorption process. *J. Chem. Phys.* **26**, 1136–1146 (1957).
32. Liu, M.-Q., Wang, C. & Kim, N.-Y. High-sensitivity and low-hysteresis porous mimtype capacitive humidity sensor using functional polymer mixed with TiO2 microparticles. *Sensors* **17**, 284 (2017).
33. Jacobs, C. B. et al. UV-activated ZnO films on a flexible substrate for room temperature O 2 and H 2 O sensing. *Sci. Rep.* **7**, 6053 (2017).
34. Tai, Y. & Lubineau, G. Human-finger electronics based on opposing humidity-resistance responses in carbon nanofilms. *Small* **13**, 1603486 (2017).
35. Jung, D., Han, M. & Lee, G. S. Humidity-sensing characteristics of multi-walled carbon nanotube sheet. *Mater. Lett.* **122**, 281–284 (2014).
36. Liu, L. et al. Humidity sensitivity of multi-walled carbon nanotube networks deposited by dielectrophoresis. *Sensors* **9**, 1714–1721 (2009).
37. Yu, S., Zhang, H., Zhang, J. & Li, Z. Effects of pH on high-performance ZnO resistive humidity sensors using one-step synthesis. *Sensors* **19**, 5267 (2019).
38. Gupta, S. P., Pawbake, A. S., Sathe, B. R., Late, D. J. & Walke, P. S. Superior humidity sensor and photodetector of mesoporous ZnO nanosheets at room temperature. *Sens. Actuators B* **293**, 83–92 (2019).
39. Dai, H., Feng, N., Li, J., Zhang, J. & Li, W. Chemiresistive humidity sensor based on chitosan/zinc oxide/single-walled carbon nanotube composite film. *Sens. Actuators B* **283**, 786–792 (2019).
40. Kalim, B. et al. CNTs/ZnO and CNTs/ZnO/Ag multilayers spray coated on cellulose fiber for use as an efficient humidity sensor. *Ceram. Int.* **46**, 25593–25597 (2020).